Figure 4. Results of FACS sorting and pyrosequencing analyses. NeuN-positive (+) are neuronal and NeuN-negative (−) are non-neuronal cells. (A) *APP*, (B) *MAPT*, (C) *GSK3B*. Two-way ANOVA and Bonferroni's multiple comparison tests revealed statistical significance. *$P < 0.05$, **$P < 0.01$, ***$P < 0.001$.
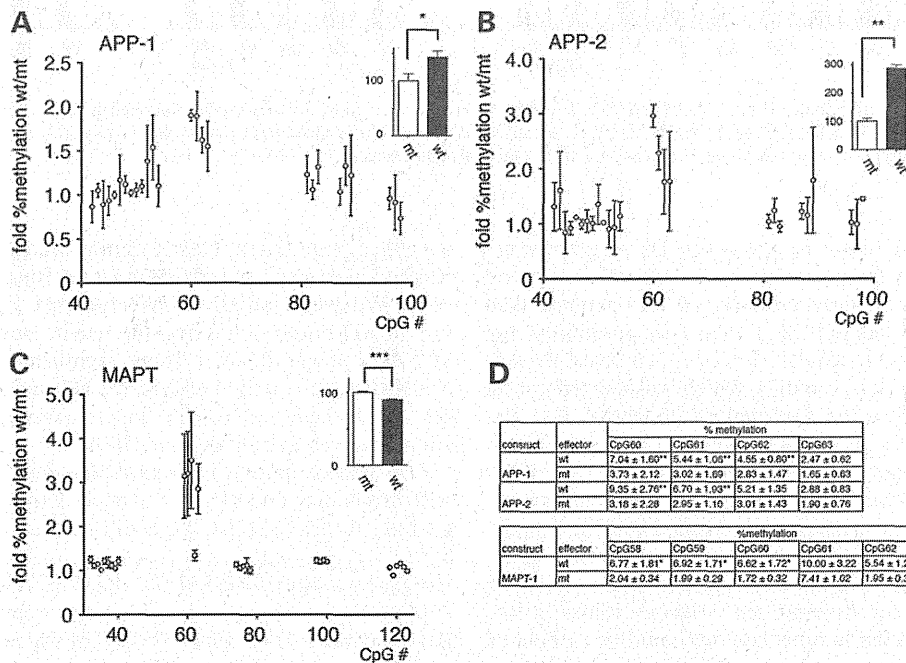

Figure 5. Results of TALE-DNMT3a construct transfection. Two different constructs coding *APP* CpGs and one against *MAPT* CpGs were transfected into 293 T cells, which were then incubated for 48 h. RNA and DNA were simultaneously extracted and subjected to qPCR and pyrosequencing. (A and B) TALE construct against *APP*. (C) TALE construct against *MAPT*. Fold % methylation was calculated as the relative value of methylation comparing the wild-type DNMT3a construct against the methylation-defective mutant. Average value from three independent experiments are shown (bar = SEM). Insets are qPCR expression assay results (DNMT V777G mutant = 100). *$P = 0.001$, **$P = 0.0020$, ***$P < 0.0001$. (D) Actual methylation measurement value (average and SD) of region of interest upon transfection of the constructs are shown. *$P < 0.05$ versus mt, **$P < 0.01$ versus mt.

Since our results are considering relatively low methylation level differences between AD and NC brains, it could raise the concern of pathological significance. For this reason, the results were further analyzed by bisulfite cloning and sequencing of *APP* and *MAPT* in a limited numbers of samples. This revealed some heavily methylated clones among fully unmethylated clones in the AD samples (Supplementary Material, Fig. S8), thus suggesting that a small percentage of abnormally methylated cells are located among normal cells in AD brains. This result supports the aggregation propagation hypothesis that proposes aggregation seed formed somewhere in the brain spreads to other areas (27), that these 'abnormally' methylated cells could serve as seed clones for aggregated protein production. Regional differences observed in this study that most of the methylation differences were observed only in the temporal lobe, where AD pathology usually begins, could also be supportive of the aggregation propagation hypothesis. Our result suggests that there are nearly 2–5% of abnormally methylated cells in the AD temporal cortex. Those

Figure 6. Subgroup analysis of the *APP* methylation status in temporal lobe samples by the presence or absence of APOE ε4 (APOE4). Overall significance was tested by two-way ANOVA and Bonferroni's multiple comparison tests, which revealed a statistically significant positive relationship *$P < 0.0001$ versus NC APOE4−, $P = 0.0333$ versus AD APOE4+, **$P = 0.0015$ versus NC APOE4−, ***$P < 0.005$ versus NC APOE4−. We analyzed 64 NC APOE4− 10 NC APOE4+, 27 AD APOE4− and 29 AD APOE4+ cases.

cells overproduce APP and MAPT, which could aggregate locally and further spread to adjacent areas of the brain where abnormal seed cells are less abundant. This is further supported by the data shown in Figure 5D that even increase in <10% methylation level can associate with expression alteration, which is due to low transfection and expression efficiency resulting in similar situation observed in the brain that a few abnormally methylated cells are present among normal cells.

Several genes are considered risk factors for AD; *APOE*, especially the ε4 genotype, confers the strongest risk. This has been shown to affect the disease pathogenesis by impairing Aβ clearance. Approximately 60% of patients with sporadic AD have this allele (28); however, possession of the ε4 allele does not guarantee that an individual will develop AD. Similarly, a significant portion of patients with AD has ε3 alleles, which does not increase the risk of dementia (29). Thus, it is of great interest to identify AD risk factors for the APOE ε4-negative population. Our results suggest a potential role of epigenetic alterations in the disease pathogenesis, especially in the APOE ε4-negative AD population. APOE is a protein related to Aβ clearance, while the E4 protein is reported to be less effective at this task (30); for this reason, it is thought to play a major role in Aβ accumulation in APOE ε4 cases. Thus, in APOE ε4-negative individuals, it may be increased APP production rather than less effective APOE that is related to the disease pathogenesis.

AD is the most prevalent neurodegenerative disease among the elderly and is characterized by the slow progressive decline in memory and executive function, both of which impair the patient's quality of life. As a result of the growing aging population in both developed and developing countries, the number of AD patients will increase dramatically by the year 2050, and the subsequent impact of this on the world economy will be disastrous (31). Existing symptomatic treatments do not change the underlying disease process or halt symptomatic progression (32). Sporadic AD pathogenesis is still unclear, but it is assumed to be somewhat similar to the FAD disease process. Here, we report a novel epigenetic alteration that specifically occurs in sporadic AD patient brains. This result pathomechanistically links FAD and sporadic AD. We hope this finding improves our
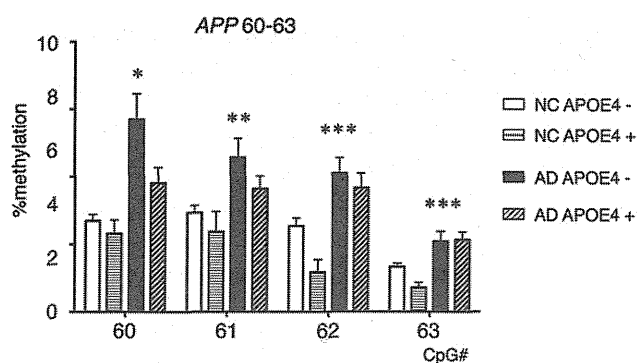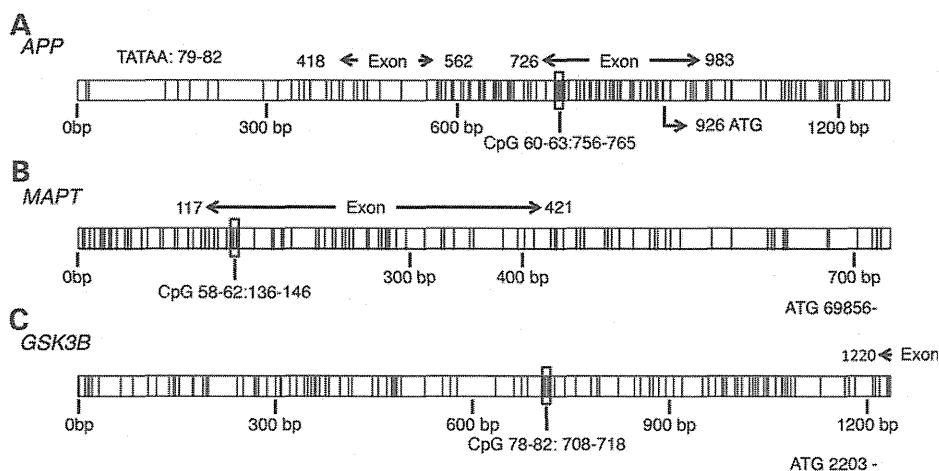

Figure 7. Structures of CpG islands analyzed in this study. Each vertical bar represents a CpG. Regions translated to mRNAs are shown as 'exon', and the first ATG positions are shown. Detected CpG regions are located below the sequences. (**A**) *APP*, (**B**) *MAPT*, (**C**) *GSK*3B.

understanding of AD and can lead to better therapies for this debilitating disease.

MATERIALS AND METHODS

Sample preparation and pyrosequencing

Post-mortem brains were obtained with written consent from patient families, and frozen at $-80°C$ until use. Fifty NC, AD and DLB subjects were obtained from Tokyo Metropolitan Geriatric Hospital brain bank, 16 NC and 10 AD were from University of Tsukuba and 30 NC and 2 AD were from the University of Tokyo. The research was approved by the ethics committee of the University of Tokyo (#2183-6). Unless otherwise noted, gray matter from the inferior temporal lobe, the superior parietal lobe and the cerebellum were excised, and DNA was extracted using the DNeasy Blood and tissue kit (Qiagen, Hilden, Germany), as according to the manufacturer's protocol. After extraction, DNA concentration was measured using a Qubit dsDNA BR assay kit (Invitrogen, Carlsbad, CA, USA). Next, 500 ng genomic DNA was subjected to the Epitect Bisulfite Kit (Qiagen) and eluted with 40 µl buffer. Next, 0.5 µl of the post-bisulfite reaction eluate was amplified via polymerase chain reaction (PCR) with a Pyromark PCR Kit (Qiagen), subjected to pyrosequencing with a Pyromark Q24 analyzer (Qiagen), and the result was analyzed with the Pyromark Q24 software (Qiagen). The list of PCR primers, sequencing primers and analysis settings are shown in Supplementary Material, Table S1. Primer sets for pyrosequencing were designed by the Pyromark Assay Design 2.0 software (Qiagen). EpiTect PCR Control DNA set (Qiagen) was used for primer calibration.

Statistical analyses

Statistical analyses were performed using the Graphpad Prism software (Graphpad Software, La Jolla, CA, USA). Statistical significance was tested by *t*-test and two-way ANOVA with Bonferroni's multiple comparison tests. Correlation analysis was tested by Pearson product-moment correlation coefficient analysis.

Neuropathological diagnosis

According to established criteria by Braak and McKeith (33–35), trained neuropathologists made diagnosis of AD, DLB or NC using hematoxylin–eosin, Nissl and silver staining, as well as immunostainings. Diagnosis of AD was based on Braak stage ≥ 3 and amyloid stage $\geq B$. DLB samples were at Lewy body score ≥ 4, Braak stage ≤ 3 and amyloid stage $\leq B$.

CpG island detection

CpG islands were detected using the CpG island searcher software (www.uscnorris.com/cpgislands/) (12).

Quantitative PCR

Cells were cultured under 5% CO_2 and 95% air, and kept at 37°C in ATCC recommended medium conditions. Cultured cells included 293, 293T, BE-(2)-C, H4, HeLa, HeLa-S3, IMR-32,

SH-SY5Y and SK-SN which were used in Supplementary Material, Figure S5 experiments. Cells were treated with TRIzol reagent (Invitrogen, Carlsbad, CA, USA) to extract RNA and DNA. A total of 1 µg total RNA per sample was reverse transcribed with Rever-Tra-ACE (Toyobo, Osaka, Japan) and analyzed by a Taqman assay using Hs00902194_m1 (*MAPT*), Hs01552283_m1 (*APP*), Hs01047719_m1 (*GSK*) and Hu GAPDH probe sets (Applied Biosystems, Foster City, CA, USA) in the 7900HT Fast Real-time PCR system (Applied Biosystems). Each individual experiments were assayed in quadruplicate and average values were used for further statistical analysis.

APOE genotyping

APOE genotyping was performed with a Taqman assay using probes C_3084793_20 and C_904973_10 (Applied Biosystems).

FACS nucleus sorting

FACS sorting was performed according to a published protocol (13). One hundred to 200 mg of brain tissue were processed to obtain 100 000–2 000 000 events following NeuN antibody staining.

TALE construct

TALE constructs were made with the TALE toolbox kit (Addgene, Cambridge, MA, USA). The target sequences for *APP* were 5′-TGCCGAGCGGGGTGGGCCGG-3′ and 5′-TGG GCCGGATCAGCTGACTC-3′. The target sequence for *MAPT* was 5′-TTCTCCTCCGGCCACTAGTG-3′. The TALE effector sequence was confirmed by direct sequencing. DNMT3a cDNA (FXC03883) was purchased from Kazusa DNA Research Institute (Kisarazu, Ciba, Japan). The V777G mutation was introduced by PCR. Transfection was performed by Lipofectamine2000 (Lifetechnologies, Carlsbad, CA, USA) following manufacturer's protocol.

SUPPLEMENTARY MATERIAL

Supplementary Material is available at *HMG* online.

ACKNOWLEDGEMENTS

FUNDING

Takeda Science Foundation (Osaka, Japan), Janssen Pharmaceutical K.K. (Tokyo, Japan) and Eisai Co. (Tokyo, Japan).

REFERENCES

1. Karran, E., Mercken, M. and De Strooper, B. (2011) The amyloid cascade hypothesis for Alzheimer's disease: an appraisal for the development of therapeutics. *Nat. Rev. Drug. Discov.*, **10**, 698–712.
2. Rovelet-Lecrux, A., Hannequin, D., Raux, G., Le Meur, N., Laquerriere, A., Vital, A., Dumanchin, C., Feuillette, S., Brice, A., Vercelletto, M. *et al.* (2006) APP Locus duplication causes autosomal dominant early-onset Alzheimer disease with cerebral amyloid angiopathy. *Nat. Genet.*, **38**, 24–26.
3. Wisniewski, K.E., Wisniewski, H.M. and Wen, G.Y. (1985) Occurrence of neuropathological changes and dementia of Alzheimer's disease in Down's syndrome. *Ann. Neurol.*, **17**, 278–282.
4. Golde, T.E., Estus, S., Usiak, M., Younkin, L.H. and Younkin, S.G. (1990) Expression of beta amyloid protein precursor mRNAs: recognition of a novel alternatively spliced form and quantitation in Alzheimer's disease using PCR. *Neuron*, **4**, 253–267.
5. Palmert, M.R., Podlisny, M.B., Golde, T.E., Cohen, M.L., Kovacs, D.M., Tanzi, R.E., Gusella, J.F., Whitehouse, P.J., Witker, D.S., Oltersdorf, T. *et al.* (1990) Analysis of the beta-amyloid protein precursor of Alzheimer's disease: mRNAs and protein products. *Adv. Neurol.*, **51**, 181–184.
6. Koo, E.H., Sisodia, S.S., Cork, L.C., Unterbeck, A., Bayney, R.M. and Price, D.L. (1990) Differential expression of amyloid precursor protein mRNAs in cases of Alzheimer's disease and in aged nonhuman primates. *Neuron*, **4**, 97–104.
7. Harrison, P.J., Wighton-Benn, W.H., Heffernan, J.M., Sanders, M.W. and Pearson, R.C. (1996) Amyloid precursor protein mRNAs in Alzheimer's disease. *Neurodegeneration*, **5**, 409–415.
8. Matsumoto, L., Takuma, H., Tamaoka, A., Kurisaki, H., Date, H., Tsuji, S. and Iwata, A. (2010) Cpg demethylation enhances alpha-synuclein expression and affects the pathogenesis of Parkinson's disease. *PLoS One*, **5**, e15522.
9. Hyman, B.T., Phelps, C.H., Beach, T.G., Bigio, E.H., Cairns, N.J., Carrillo, M.C., Dickson, D.W., Duyckaerts, C., Frosch, M.P., Masliah, E. *et al.* (2012) National Institute on Aging-Alzheimer's Association guidelines for the neuropathologic assessment of Alzheimer's disease. *Alzheimers Dement.*, **8**, 1–13.
10. Montine, T.J., Phelps, C.H., Beach, T.G., Bigio, E.H., Cairns, N.J., Dickson, D.W., Duyckaerts, C., Frosch, M.P., Masliah, E., Mirra, S.S. *et al.* (2012) National Institute on Aging-Alzheimer's Association guidelines for the neuropathologic assessment of Alzheimer's disease: a practical approach. *Acta Neuropathol.*, **123**, 1–11.
11. De Strooper, B., Vassar, R. and Golde, T. (2010) The secretases: enzymes with therapeutic potential in Alzheimer disease. *Nat. Rev. Neurol.*, **6**, 99–107.
12. Takai, D. and Jones, P.A. (2003) The CpG island searcher: a new WWW resource. *In Silico Biol.*, **3**, 235–240.
13. Iwamoto, K., Bundo, M., Ueda, J., Oldham, M.C., Ukai, W., Hashimoto, E., Saito, T., Geschwind, D.H. and Kato, T. (2011) Neurons show distinctive DNA methylation profile and higher interindividual variations compared with non-neurons. *Genome Res.*, **21**, 688–696.
14. Boch, J., Scholze, H., Schornack, S., Landgraf, A., Hahn, S., Kay, S., Lahaye, T., Nickstadt, A. and Bonas, U. (2009) Breaking the code of DNA binding specificity of TAL-type III effectors. *Science*, **326**, 1509–1512.
15. Moscou, M.J. and Bogdanove, A.J. (2009) A simple cipher governs DNA recognition by TAL effectors. *Science*, **326**, 1501.
16. Sanjana, N.E., Cong, L., Zhou, Y., Cunniff, M.M., Feng, G. and Zhang, F. (2012) A transcription activator-like effector toolbox for genome engineering. *Nat. Protoc.*, **7**, 171–192.
17. Gowher, H. and Jeltsch, A. (2002) Molecular enzymology of the catalytic domains of the Dnmt3a and Dnmt3b DNA methyltransferases. *J. Biol. Chem.*, **277**, 20409–20414.
18. Barrachina, M. and Ferrer, I. (2009) DNA Methylation of Alzheimer disease and tauopathy-related genes in postmortem brain. *J. Neuropathol. Exp. Neurol.*, **68**, 880–891.
19. Wang, S.C., Oelze, B. and Schumacher, A. (2008) Age-specific epigenetic drift in late-onset Alzheimer's disease. *PLoS One*, **3**, e2698.
20. Rogaev, E.I., Lukiw, W.J., Lavrushina, O., Rogaeva, E.A. and St George-Hyslop, P.H. (1994) The upstream promoter of the beta-amyloid precursor protein gene (APP) shows differential patterns of methylation in human brain. *Genomics*, **22**, 340–347.
21. Grunau, C., Clark, S.J. and Rosenthal, A. (2001) Bisulfite genomic sequencing: systematic investigation of critical experimental parameters. *Nucleic. Acids. Res.*, **29**, e65.
22. Warnecke, P.M., Stirzaker, C., Song, J., Grunau, C., Melki, J.R. and Clark, S.J. (2002) Identification and resolution of artifacts in bisulfite sequencing. *Methods*, **27**, 101–107.
23. Gius, D., Cui, H., Bradbury, C.M., Cook, J., Smart, D.K., Zhao, S., Young, L., Brandenburg, S.A., Hu, Y., Bisht, K.S. *et al.* (2004) Distinct effects on gene expression of chemical and genetic manipulation of the cancer epigenome revealed by a multimodality approach. *Cancer Cell*, **6**, 361–371.
24. Suzuki, M.M. and Bird, A. (2008) DNA Methylation landscapes: provocative insights from epigenomics. *Nat. Rev. Genet.*, **9**, 465–476.
25. Jones, P.A. (2012) Functions of DNA methylation: islands, start sites, gene bodies and beyond. *Nat. Rev. Genet.*, **13**, 484–492.
26. Lee, V.M. and Trojanowski, J.Q. (1992) The disordered neuronal cytoskeleton in Alzheimer's disease. *Curr. Opin. Neurobiol.*, **2**, 653–656.
27. Frost, B. and Diamond, M.I. (2010) Prion-like mechanisms in neurodegenerative diseases. *Nat. Rev. Neurosci.*, **11**, 155–159.
28. Verghese, P.B., Castellano, J.M. and Holtzman, D.M. (2011) Apolipoprotein E in Alzheimer's disease and other neurological disorders. *Lancet Neurol.*, **10**, 241–252.
29. Liu, C.C., Kanekiyo, T., Xu, H. and Bu, G. (2013) Apolipoprotein E and Alzheimer disease: risk, mechanisms and therapy. *Nat. Rev. Neurol.*, **9**, 106–118.
30. Castellano, J.M., Kim, J., Stewart, F.R., Jiang, H., DeMattos, R.B., Patterson, B.W., Fagan, A.M., Morris, J.C., Mawuenyega, K.G., Cruchaga, C. *et al.* (2011) Human apoE isoforms differentially regulate brain amyloid-beta peptide clearance. *Sci. Transl. Med.*, **3**, 89ra57.
31. Wimo, A. and Price, M. (2010) World Alzheimer Report 2010. *Alzheimer's Disease International*, 1–54.
32. Iwata, A. and Iwatsubo, T. (2013) Disease-modifying therapy for Alzheimer's disease: challenges and hopes. *Neurol. Clin. Neurocience*, **1**, 49–54.
33. Braak, H. and Braak, E. (1991) Demonstration of amyloid deposits and neurofibrillary changes in whole brain sections. *Brain Pathol.*, **1**, 213–216.
34. McKeith, I.G., Galasko, D., Kosaka, K., Perry, E.K., Dickson, D.W., Hansen, L.A., Salmon, D.P., Lowe, J., Mirra, S.S., Byrne, E.J. *et al.* (1996) Consensus guidelines for the clinical and pathologic diagnosis of dementia with Lewy bodies (DLB): report of the consortium on DLB international workshop. *Neurology*, **47**, 1113–1124.
35. Braak, H. and Braak, E. (1991) Neuropathological stageing of Alzheimer-related changes. *Acta Neuropathol.*, **82**, 239–259.

ACTA NEUROPATHOLOGICA
COMMUNICATIONS

RESEARCH   Open Access

Ultrastructural differences in pretangles between Alzheimer disease and corticobasal degeneration revealed by comparative light and electron microscopy

Shinsui Tatsumi[1,2,3], Toshiki Uchihara[2*], Ikuko Aiba[4], Yasushi Iwasaki[1], Maya Mimuro[1], Ryosuke Takahashi[3] and Mari Yoshida[1]

Abstract

Pretangles are defined under the light microscope as diffuse and granular tau immunoreactivity in neurons in tissue from patients with Alzheimer disease (AD) or corticobasal degeneration (CBD) and are considered to be a premature stage before neurofibrillary tangle formation. However, the ultrastructure of pretangles remains to be described. To clarify the similarities and differences between pretangles from patients with AD and CBD (AD-pretangles and CBD-pretangles, respectively), we examined cortical pretangles in tissue from patients with each of diseases. For direct light and electron microscopic (LM/EM) correlation of the pretangles, we used quantum dot nanocrystals (QDs) with dual fluorescent and electron-dense properties. We first identified tau-labeled pretangles on fluorescence LM and subsequently examined the same neurons on EM. Energy dispersive X-ray spectrometry (EDX) color mapping identified selenium (Se) and cadmium (Cd) as elementary components of QDs and highlighted each QD particle clearly against gray-scale EM images. With these methods, we were successful for the first time in demonstrating accurately that LM-defined pretangles are tau-positive straight filaments sparsely distributed throughout neuronal cytoplasm and neurites in both AD and CBD at the EM level. Notably, AD-pretangles showed a strong tendency to form fibrillary tangles even at an early stage, whereas pretangles or Pick-like inclusions in tissue from patients with CBD did not even at an advanced stage. In conclusion, AD-pretangles and CBD-pretangles showed essential differences at the EM level.

Introduction

Changes that occur in relevant molecules before they become organized into disease-specific inclusions in human brains are attracting increasing attention [1]. The pretangle is an example of such an early change; it was originally defined under light microscopy (LM) as diffuse and granular tau immunoreactivity in the cytoplasm and neurites of otherwise intact neurons in brains from patients with Alzheimer disease (AD) [2-4]. Mature neurofibrillary tangles (NFTs), which are hallmarks of AD, are readily identified as bundles of paired helical filaments (PHFs) under electron microscopy (EM) [5]. However, it is difficult to identify pretangles under EM because their faint tau immunoreactivity suggests that their ultrastructure is less distinct. Although putative ultrastructures of pretangles in AD have been reported, it is not yet clarified whether they really represent neurons containing diffuse and granular tau immmunoreactivity as defined under LM [2]. Similar granular tau immunoreactivity has also been observed in corticobasal degeneration (CBD), a four-repeat tauopathy that causes degeneration of the cerebral cortex, basal ganglia, and substantia nigra. Because they appear similar to AD-pretangles under LM, this granular tau immunoreactivity is also known as pretangles. Pretangles are considered one of the most important neuronal cytopathologies in CBD [6,7] but are also found in argyrophilic grain disease or progressive supranuclear palsy [8].

* Correspondence: uchihara-ts@igakuken.or.jp
[2]Laboratory of Structural Neuropathology, Tokyo Metropolitan Institute of Medical Science, 2-1-6 Kamikitazawa, Setagaya, Tokyo 156-8506, Japan
Full list of author information is available at the end of the article

The aim of this study was to visualize the ultrastructures of LM-defined AD- and CBD-pretangles and thereby to identify possible differences between them. For this purpose, it is necessary to directly compare LM and EM images of the same pretangle, an approach that is now named "correlative light and electron microscopy (CLEM)". Although CLEM protocols have been developing [9-17], they usually allow LM/EM comparisons for only small fields (the size of the EM preparation). This limitation makes it practically impossible to capture pretangles for immunoEM study because pretangles are not sufficiently frequent to be included by chance in such tiny preparations. Therefore, it is necessary to excise tissue containing a pretangle from the LM sample before it can be prepared for EM.

Quantum dots (QDs) are fluorescent, electron-dense semiconductor nanocrystals of uniform size with a core of cadmium selenide [18]. On EM examination, QDs also display a characteristic peripheral halo [19]. These dual optical properties allow QDs to be identified under both LM and EM and therefore permits labeled LM structures to be compared directly with their ultrastructures [16]. Using QDs, we recently established three dimension (3D) - oriented immunoelectron microscopy [19,20]. In this method, a thick floating section from the formalin-fixed human brain is incubated with the primary and QD-conjugated secondary antibodies. After a target neuron is examined with fluorescent LM (confocal microscopy), landmarks are punched out around the neuron using laser microdissection. Then, this floating section is processed for EM preparation. The advantage of this stepwise LM-EM approach is that the neuron of interest can be observed closely on confocal microscopy prior to the EM examination, and its EM findings can be supplemented with confocal images because the same reporter (i.e., QDs) can been seen under both LM and EM immunostaining.

Although QDs provide a powerful bridge between LM and EM, their electron density is lower and their contour is less distinct than those of gold particles, leading to doubts about QD use as an immunolabeling material for EM. We previously overcame this problem using energy dispersive X-ray (EDX) spectrometry, which demonstrated parallel peaks corresponding to selenium (Se) and cadmium (Cd) on the pixels for definitive confirmation of QDs on EM preparations [19]. Because it is possible to obtain EDX spectrum for each pixel, we extended this pixel-based EDX analysis to plot the entire EM field pixel by pixel in this study. Operational display of pixels containing Cd peak or those containing Se peak highlighted QD particles based on their elemental composition with different colors. When it was overlaid onto the conventional gray-scale EM image, this EDX color mapping clearly distinguished QDs from background structures such as ribosomes.

With these methods, it is possible to examine the ultrastructural details of AD- and CBD-pretangles and to elucidate their similarities and differences at the EM level [2-4,6]. Using this LM/EM correlation with novel mapping method, we obtained an EM image of the early stage of neuronal tau deposition in AD-pretangles and found essential differences between AD- and CBD-pretangles at the EM level. This is the first successful demonstration of their ultrastructural differences.

Materials and methods
Alzheimer disease and corticobasal degeneration cases
To investigate the ultrastructure of pretangles, we compared them in different diseases with different severities (Table 1). We used samples from one case of AD, a case of normal aging, and two typical cases of CBD. The diagnoses of AD and CBD were based on the current diagnostic criteria [6,21]. Identification of pretangles was based on LM findings as "cytoplasmic diffuse and granular tau immunoreactivity without apparent fibrillary structures". In the normal aging samples, pretangles and Alzheimer-type NFTs were localized to the hippocampus and the parahippocampal cortex. In the CBD samples, we examined

Table 1 Demographic features of cases with AD, normal aging, and CBD

	Pathological diagnosis	Age of death (y)/sex	Brain weight (g)	Duration (y)	Braak NFT stage	Clinical symptoms	Type of tau-positive inclusions investigated
Case 1	Normal aging	73/F	1,260	na	I	No history of dementia or motor symptoms	Pretangles, NFTs
Case 2	AD	58/F	850	14	VI	Severe dementia, disorientation	Pretangles, NFTs
Case 3	CBD	60/M	1,145	7	I	Supranuclear gaze palsy, frequent fall, parkinsonism, frontal signs	Pretangles, Pick-like inclusions*
Case 4	CBD	70/F	770	11	III	Frontotemporal dementia, parkinsonism	Pretangles, Pick-like inclusions, ballooned neurons

*Pick-like inclusions denoting densely packed round inclusions usually observed in the small-sized cortical neurons in corticobasal degeneration; AD, Alzheimer disease; CBD, corticobasal degeneration; NFT, neurofibrillary tangle.

pretangles and densely packed round inclusions (Pick-like inclusions) [6] in the frontal lobe.

Pre-embedding tau/QD labeling for LM/EM observation

Formalin-fixed brains were rinsed in phosphate-buffered saline (PBS) and cryoprotected in 20% sucrose/PBS overnight. The tissue was frozen in optimal cutting temperature (OCT) compound and cut into 25-μm-thick floating sections on a freezing microtome. The sections were immersed in 1% bovine serum albumin/PBS for 30 min and then incubated in anti-PHF tau antibody (AT8, mouse, monoclonal, 1:700; Thermo Fisher Scientific, Tokyo, Japan) for 24 hours at room temperature (RT). After washing in PBS for 30 min, sections were incubated in an anti-mouse secondary antibody conjugated to Q-dot 655 (QD 655) (goat, 1:100 to 1:800, diluted in PBS; Invitrogen, Carlsbad, CA) for 8 hours at RT. A QD 655 dilution at 1:400 (Additional file 1: Figure S1) for a CBD pretangle provided appropriate immunoEM labeling on tau-positive filaments, whereas its fluorescent signal was not intense enough to delineate subcellular details under confocal microscopy (Additional file 1: Figure S1). Therefore, the QD-labeled sections were subsequently incubated in an anti-mouse secondary antibody conjugated to Alexa 488 (goat, 1:200; Molecular Probe) for 3 hours at RT to allow more detailed LM observation. After incubation, sections were rinsed in PBS and then mounted in fluorescence-mounting medium (S3023; Dako, Glostrup, Denmark).

Confocal LM observation and EM preparation

Three-dimensional reconstruction images of the pretangles were obtained under fluorescence confocal microscopy (LSM 710; Carl Zeiss, Oberkochen, Germany) using a 63 × –oil immersion objective lens. Alexa 488 was excited using an argon laser (488 nm), and the detection bandwidth was set at 493 to 601 nm (expected peak at 520 nm). QD 655 was excited with a diode laser (405 nm), and the detection bandwidth was set at 605 to 690 nm (expected peak at 655 nm), which gave essentially the same image as obtained with Alexa 488 [19]. A Z-series scan (800 × 800 pixels, interval 0.40 μm, approximately 10-μm thick in total) was performed for 3D reconstruction. After obtaining 3D data sets with the confocal microscope, landmarks were punched out around the target neurons using the UV laser Micro dissection system PALM (P.A.L.M. Microlaser Technologies, Bernried, Germany) (Figure 1). The sections were then detached from the glass slide, fixed in 2% glutaraldehyde for 10 min, and postfixed in 1% osmium tetroxide for 30 min. Next, the sections were embedded in epon as follows: they were gently pressed between aclar films (Nissin EM catalog #4513, Tokyo, Japan) so that flat preparation on epon was possible and then hardened

with heat (60°C). An aclar film on one side was detached from the hardened epon-embedded section. Then, the section was stuck to columnar epon that had been prepared in advance (Figure 1). The target-oriented trimming of the epon block was facilitated by the guidance of punched out landmarks around the target already identified and 3D-reconstructed on confocal microscopy. Ultrathin sections of the trimmed blocks were stained with uranyl acetate/lead citrate and examined with a JEM-1400 electron microscope (JEOL, Tokyo, Japan). After obtaining the most appropriate EM images, their exact LM counterpart was retrieved from the corresponding fluorescent 3D data set for direct comparison (Figure 1).

Energy dispersive X-ray (EDX) spectrometry and elemental mapping of QDs

The EM sections were also observed under a Hitachi HD-2700 scanning transmission electron microscope (STEM, Hitachi High Technologies Corporation, Tokyo, Japan). This STEM is equipped with a cold-field emission gun and detectors that consist of bright-field, high-angle annular dark-field (HAADF) and secondary electron (SE) detectors, which distinguish different elements (Cd and Se in this experiment) based on their energy spectra on a pixel basis. This approach identifies the presence of Cd and Se in each STEM pixel. This pixel-based identification of Cd and Se is then extended to map the entire EM field to delineate the QD particles in relation to underlying ultrastructures. The STEM was operated at 200 kV and an EDX spot analysis was performed with an incident beam size of 0.2 nm and a current of 0.4 nA. The acquisition time for each pixel was 200 μsec. In the EDX mapping, the EDX analysis was performed in a 0.4 μm × 0.5 μm field, and the total acquisition time was 90 min. Pixels containing Se or Cd peaks were displayed on the EM field independently in different color channels.

Results

EDX analysis and EDX mapping of QDs

The shape of electron-dense QD 655, dribbled on the formvar membrane, was spherical to oblong on the STEM image (Additional file 2: Figure S2A). Pixel-based EDX elementary mapping highlighted the distribution of Se and Cd (Additional file 2: Figure S2B and D, respectively), which exactly corresponded to the ultrastructural shape of QDs (Additional file 2: Figure S2C). In a CBD-pretangle (case 3) examined using a QD 655-conjugated secondary antibody, tau filaments were labeled with numerous QDs of similar morphology (Figure 2A). The EDX spot analysis identified these QDs on the basis of energy peaks corresponding to Se and Cd. Elemental mapping with this EDX analysis further showed the distribution of QDs based on the presence of Se and Cd (Figure 2B). As mentioned, when the original STEM image was overlaid onto this
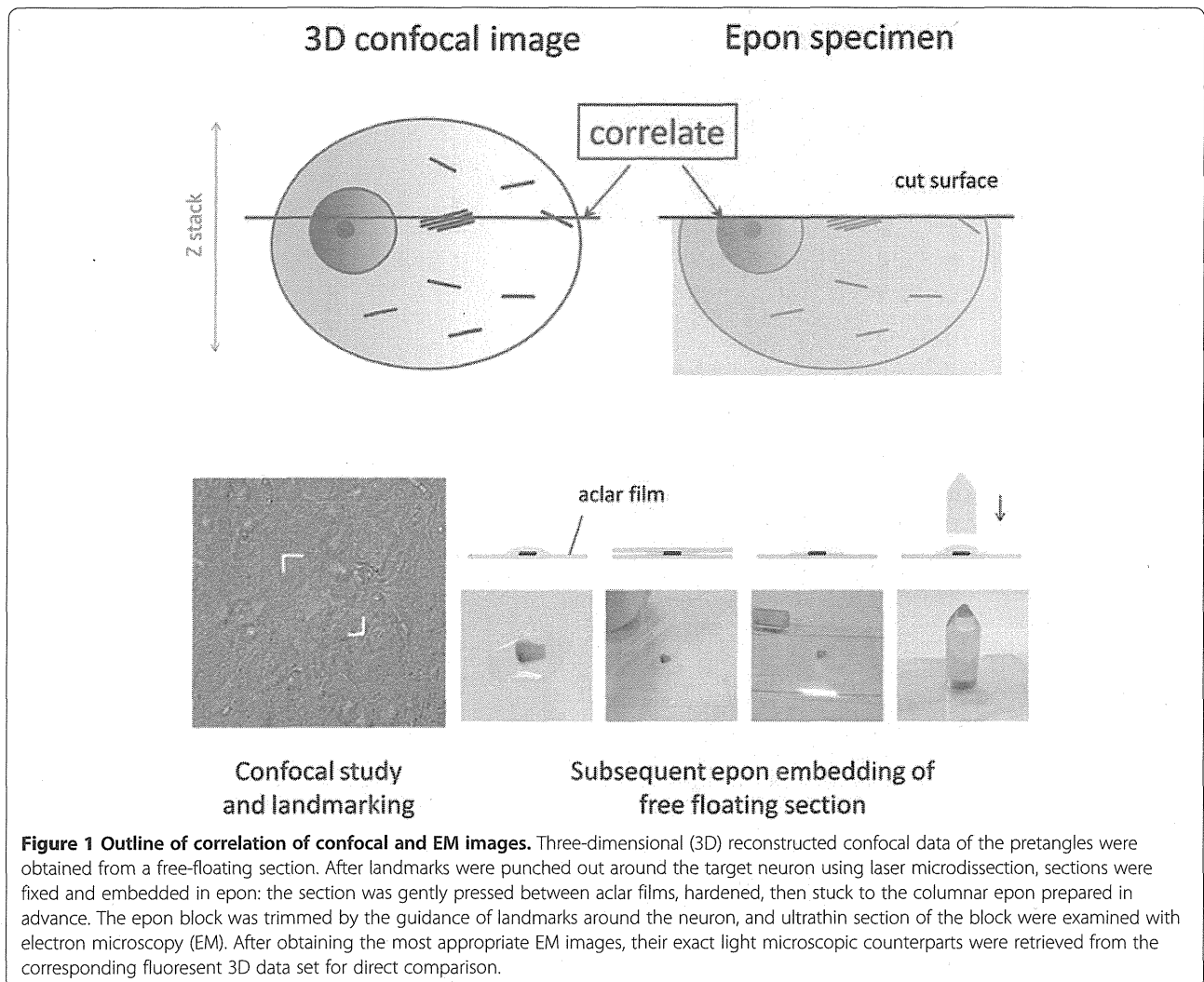
Figure 1 Outline of correlation of confocal and EM images. Three-dimensional (3D) reconstructed confocal data of the pretangles were obtained from a free-floating section. After landmarks were punched out around the target neuron using laser microdissection, sections were fixed and embedded in epon: the section was gently pressed between aclar films, hardened, then stuck to the columnar epon prepared in advance. The epon block was trimmed by the guidance of landmarks around the neuron, and ultrathin section of the block were examined with electron microscopy (EM). After obtaining the most appropriate EM images, their exact light microscopic counterparts were retrieved from the corresponding fluoresent 3D data set for direct comparison.

EDX mapping, the regional distributions of these analytical QD signals were identical to the ultrastructural shapes of QDs (Figure 2C). With this technique, the QDs could be readily differentiated from the grayscale background, even if the tau-filaments were intermingled with (similarly round) ribosomes (Figure 2C, arrow).

LM findings and corresponding ultrastructures of pretangles in AD and aging

Confocal examination of AD-pretangles revealed a mixture of granular tau immunoreactivity and small tangle formation (Figure 3A, stacked 3D image). When an EM section (C) and the corresponding LM counterpart on the same plane (B) were compared, the tangle-like aggregate (B, arrow; C, rectangle d) was found to be a small bundle of straight filaments tightly arranged in parallel (D), which is indistinguishable from mature NFTs in AD (Figure 3B-D). Such a precise comparison on the corresponding planes of LM and EM was not possible between

3D stacked image (A) and the EM section (C). In contrast, granular immunoreactivity on the LM plane (B), corresponded to straight filaments randomly and sparsely distributed throughout the cytoplasm (arrowheads, E), probably representing an earlier stage before bundle formation (Figure 3B, C, E). Occasional paired helical filaments (PHFs) were observed in AD-pretangles (Figure 3F). The distribution of these tau filaments was so sparse that they could be identified on EM only with dual guidance through subcellular orientation using a LM image and QD immunolabeling. Perinuclear staining was sometimes found in AD-pretangles on confocal images (G: stacked 3D image and corresponding plane on LM (H) and EM (I)). This corresponded to a low density of immunolabeled straight filaments attached to the nuclear membrane (Figure 3I, J, asterisk). The diameter of straight filaments ranged from 14 to 16 nm, and the period of filament constriction was 70 to 90 nm in AD and normal aging cases.
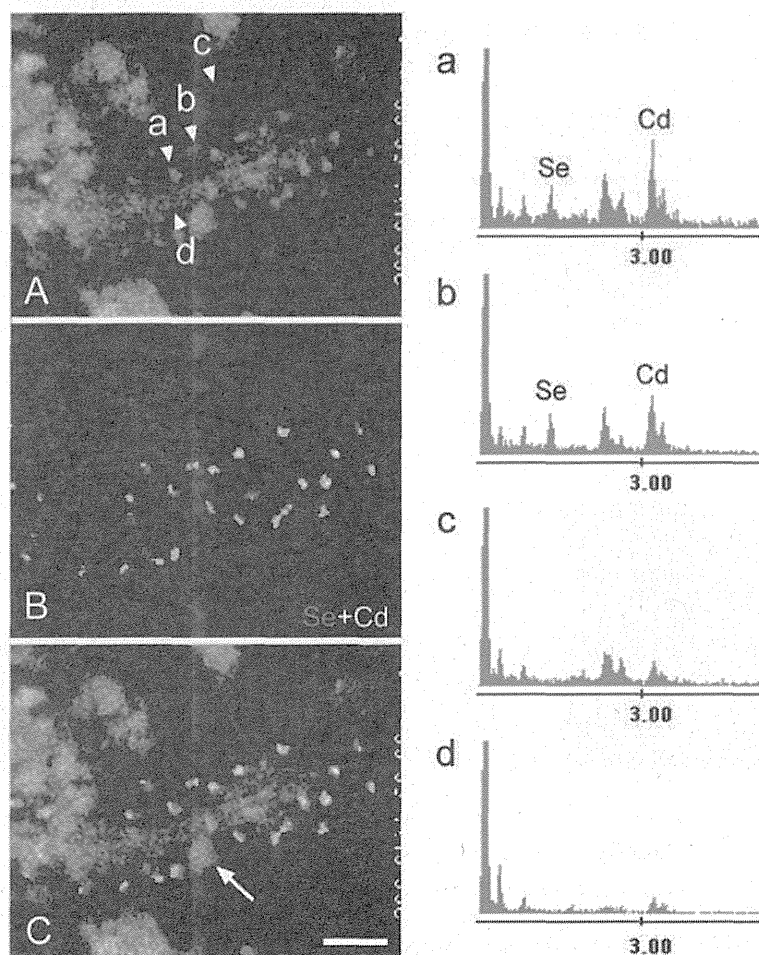
Figure 2 EDX mapping of QDs around tau-positive straight filaments in a case of CBD. EDX spot analysis of the section highlighted energy peaks corresponding to Se and Cd on QDs (Arrowheads **a** and **b** in panel **A** correspond to energy spectra **a** and **b**), but not on the background (arrowhead **c**) and the filament itself (arrowhead **d**). This pixel-based identification of Cd and Se is then extended to map the entire EM field to delineate the QD particles in relation to underlying ultrastructures. This approach produced Se (pink)- and Cd (yellow)-specific signals derived from QDs (**B**) as a map independent of underlying ultrastructures. The QDs were easily distinguished from a ribosome (arrow) (overlay, **C**). Scale bar = 50 nm.
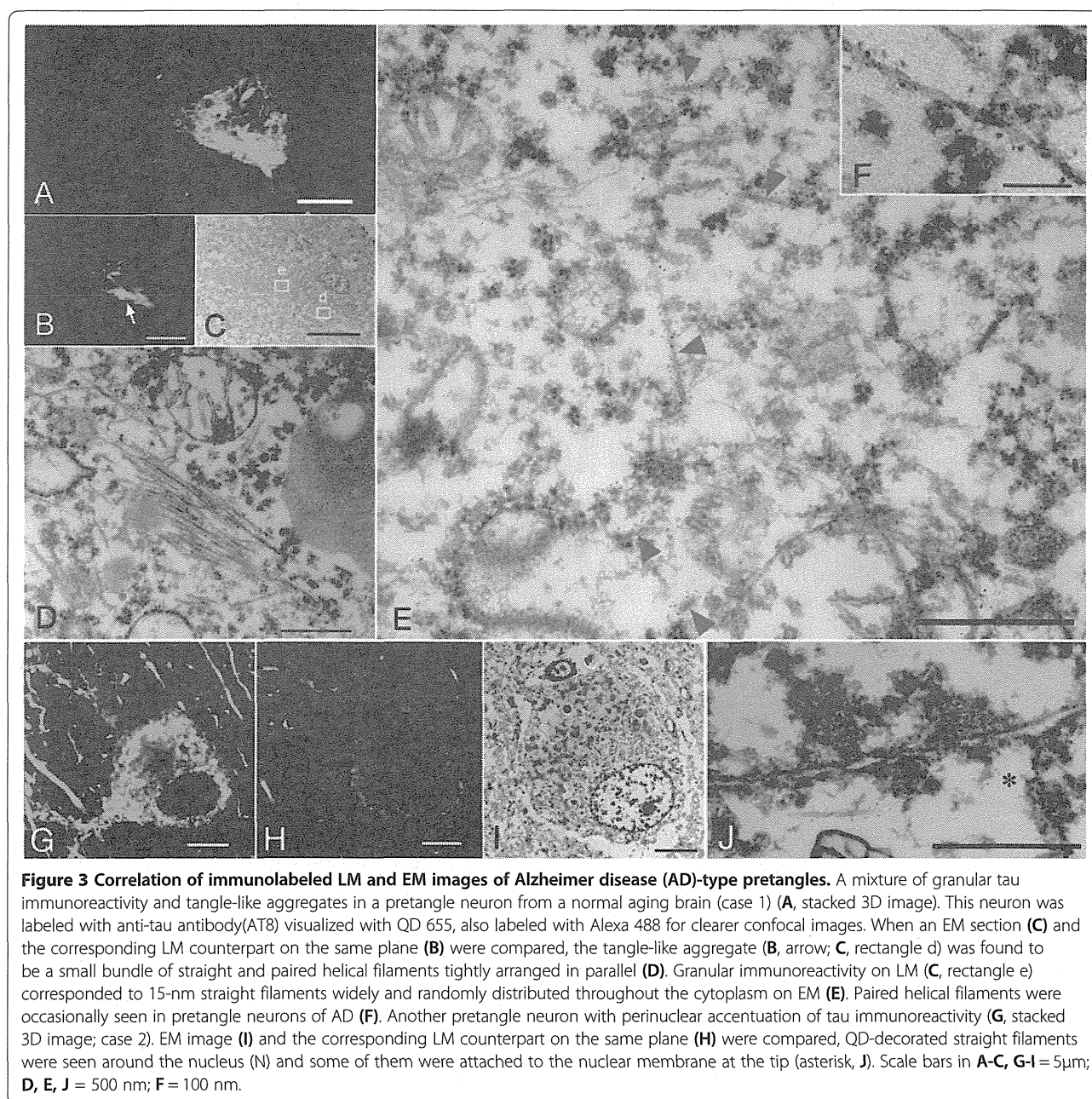
LM findings and corresponding ultrastructures of CBD-pretangles

CBD-pretangles, which were often found in the superficial and deep layers of the cerebral cortex, were characterized by diffuse and reticular (rather than granular) immunoreactivity in the neuronal cytoplasm with few solid aggregates (Figure 4A). The density of the reticular structures varied from cell to cell or from case to case. 3D observations using confocal microscopy showed that the reticular structures extended into the distal portions of dendrites (Figure 4A). Perinuclear tau immunoreactivity, as seen in AD-pretangles, was not observed in CBD-pretangles. Correlation of the LM and EM images demonstrated that reticular structures seen by confocal microscopy corresponded to straight filaments, which were diffusely and randomly distributed throughout the cytoplasm and did not displace cellular organellae

(Figure 4A-C, E). In dendrites, a few straight filaments were assembled in a roughly parallel fashion. Their arrangement was less tight than in NFTs in AD (Figure 4D). In tissue from the more severe case of CBD (case 4), reticular structures were denser on both confocal microscopy and EM images than in case 3 (Figure 5A- E). Interestingly, straight filaments were thicker in diameter in case 4 (15–20 nm) than in case 3 (14 to 15 nm). Straight filaments also appeared longer in case 4. In this study, PHFs were not observed in CBD-pretangles in either case.

Ultrastructure of Pick-like inclusions in small neurons in two CBD cases

Densely packed round inclusions (Pick-like inclusions) were found mainly in the small neurons in the superficial layer of the cerebral cortex of CBD cases; their tau

Figure 3 Correlation of immunolabeled LM and EM images of Alzheimer disease (AD)-type pretangles. A mixture of granular tau immunoreactivity and tangle-like aggregates in a pretangle neuron from a normal aging brain (case 1) (**A**, stacked 3D image). This neuron was labeled with anti-tau antibody(AT8) visualized with QD 655, also labeled with Alexa 488 for clearer confocal images. When an EM section (**C**) and the corresponding LM counterpart on the same plane (**B**) were compared, the tangle-like aggregate (**B**, arrow; **C**, rectangle d) was found to be a small bundle of straight and paired helical filaments tightly arranged in parallel (**D**). Granular immunoreactivity on LM (**C**, rectangle e) corresponded to 15-nm straight filaments widely and randomly distributed throughout the cytoplasm on EM (**E**). Paired helical filaments were occasionally seen in pretangle neurons of AD (**F**). Another pretangle neuron with perinuclear accentuation of tau immunoreactivity (**G**, stacked 3D image; case 2). EM image (**I**) and the corresponding LM counterpart on the same plane (**H**) were compared, QD-decorated straight filaments were seen around the nucleus (N) and some of them were attached to the nuclear membrane at the tip (asterisk, **J**). Scale bars in **A-C, G-I** = 5μm; **D, E, J** = 500 nm; **F** = 100 nm.

immunoreactivity was more compact and denser than that of CBD-pretangles. On confocal observation, we found that these inclusions often contained small cavities (Figure 6A-B). The correlation of LM and EM images revealed bundles of tau filaments around the cavities (Figure 6B-D). Tau-positive filaments were composed of straight filaments and PHFs with a periodicity of approximately 130 nm (Figure 6D-E). These filaments were loosely assembled and usually intermingled with cellular organellae, especially ribosomes (Figure 6D, arrow). Strictly speaking, the straight filaments were

not oriented parallel to each other. The diameters of straight filaments in these inclusions ranged from 13 to 15 nm in case 3 and 15 to 16 nm in case 4. Similarities and differences among AD-pretangles, NFTs in AD, CBD-pretangles, and Pick-like inclusions in CBD are listed in Table 2.

Among hundreds of AT8-positive neurons on confocal, 3–4 pretangles were selected in each AD and CBD case, which were 3D-reconstructed and prepared for EM observation. In addition, 3–4 Pick-like inclusions were selected in each CBD case and were processed similarly.